Journal of Controlled Release 367 (2024) 184–196

Contents lists available at ScienceDirect

Journal of Controlled Release

journal homepage: www.elsevier.com/locate/jconrel

Dual engine-driven bionic microneedles for early intervention and prolonged treatment of Alzheimer's disease

Minmin Zhang [a,b,1], Beibei Yang [a,1], Tao Ren [c], Xuewen Wang [c], Hangping Chen [c], Chao Lu [c], Chuanbin Wu [c], Xin Pan [a], Tingting Peng [b,c,*]

[a] School of Pharmaceutical Sciences, Sun Yat-sen University, Guangzhou 510006, PR China
[b] State Key Laboratory of Bioactive Molecules and Druggability Assessment, Jinan University, Guangzhou 511436, China
[c] International Cooperative Laboratory of Traditional Chinese Medicine Modernization and Innovative Drug Development of Ministry of Education (MOE) of China/ College of Pharmacy, Jinan University, Guangzhou 511436, China

ARTICLE INFO

Keywords:
Gas-propelled microneedle
Biomimetic structure
Drug delivery system
Transdermal delivery efficiency
Rivastigmine
Alzheimer's disease

ABSTRACT

The microneedle (MN) delivery system presents an attractive administration route for patients with Alzheimer's disease (AD). However, the passive drug delivery mode and low drug loading of MNs often result in unsatisfactory therapeutic efficiency. To address these dilemmas, we developed dual engine-drive bionic MNs for robust AD treatment. Specifically, free rivastigmine (RVT) and RVT particles were co-loaded within the MNs to construct the valve and chambers of the guava, respectively, which can serve as an active engine to promote drug permeation by generating capillary force. K_2CO_3 and citric acid were introduced as a pneumatic engine into the MNs to promote the permeation of free RVT into deeper skin layers for early intervention in AD. Further, the RVT particles served as a drug depot to provide continuous drug release for prolonged AD treatment. Compared with free RVT-loaded MNs, the dual engine-driven bionic MNs showed an increase in drug loading, cumulative transdermal permeability, and normalized bioavailability of approximately 40%, 22%, and 49%, respectively. Pharmacodynamic studies further confirmed that the dual engine-driven bionic MNs were most effective in restoring memory and recognition functions in mice with short-term memory dysfunction. Therefore, the dual engine-driven bionic MNs hold great promise for highly efficient AD treatment.

1. Introduction

Alzheimer's disease (AD) is an irreversible neurodegenerative disorder that typically affects individuals aged 65 and older [1,2]. Its clinical manifestations include memory, vision, and executive function impairment; language and cognitive decline; and personality and behavior alternations. These symptoms significantly decrease patients' quality of life [3,4]. According to the World Health Organization's 2018 report on AD, dementia has become a global crisis. In 2018, there were approximately 50 million patients with AD worldwide, a number projected to increase to 82 million by 2030 and 152 million by 2050 [5]. The global cost of AD has surpassed that of heart disease, cancer, and stroke and is expected to reach $2 trillion by 2030, placing a significant economic burden on the society. Therefore, there is an urgent need to develop an effective drug delivery system for improved treatment of AD.

Rivastigmine (RVT) is the first-line treatment for mild-to-moderate AD [6,7]. RVT is a carbamate-selective acetylcholinesterase inhibitor developed by Novartis and approved for marketing by the FDA in May 1998 [8,9]. It promotes cholinergic neurotransmission by delaying the degradation of acetylcholine released from functionally intact cholinergic neurons [10]. Currently, RVT is clinically available in several dosage forms, including capsules, tablets, oral solutions, and transdermal patches. Oral administration of RVT often leads to gastrointestinal side effects, such as nausea, vomiting, abdominal pain, loss of appetite, and weight loss [11]. In particular, the senile patients may have swallowing difficulties and find the consumption of conventional tablets or capsules challenging. Although transdermal patches, such as Exelon, effectively mitigate the gastrointestinal side effects of oral medications, their therapeutic efficacy is still hindered by low transdermal delivery efficiency due to the rigid stratum corneum barrier. For continuous treatment, Exelon must be applied to the skin for extended periods, up to 24 h, which usually causes skin itching and ulceration, as

* Corresponding author at: College of Pharmacy, Jinan University, Guangzhou 511436, China.
E-mail address: pengtt@jnu.edu.cn (T. Peng).
[1] These authors contributed equally to this work.

https://doi.org/10.1016/j.jconrel.2024.01.030
Received 8 October 2023; Received in revised form 25 December 2023; Accepted 15 January 2024
Available online 26 January 2024

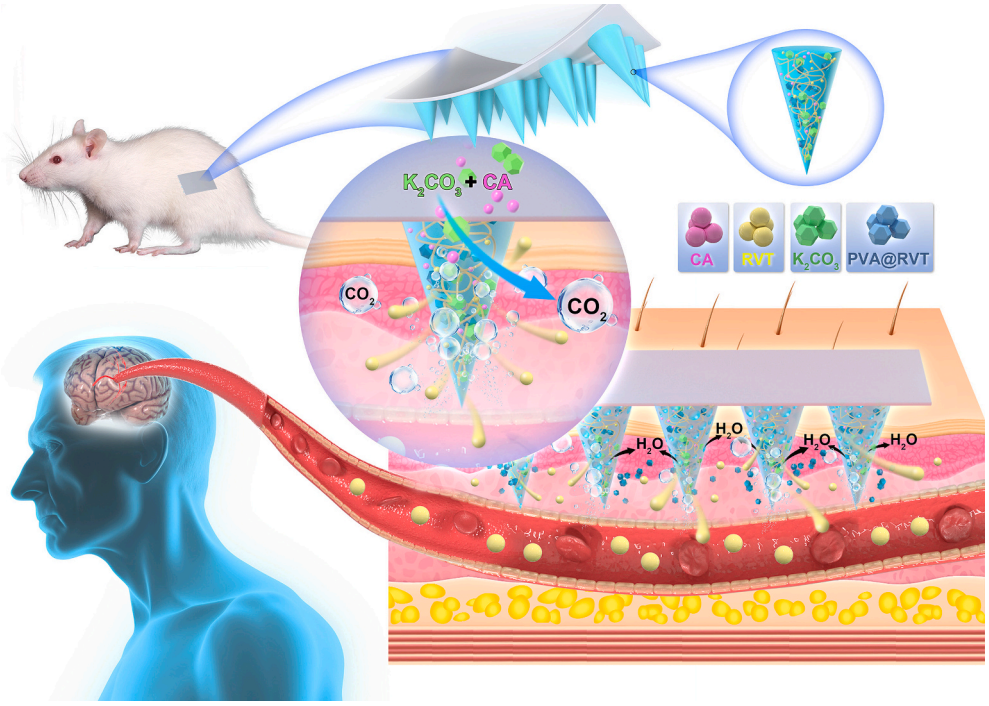

Fig. 1. Schematic illustration of guava-bioinspired gas-propelled MNs for the early intervention and prolonged treatment of AD.

well as considerable discomfort to the patients [12–14].

Dissolving microneedles (MNs) have emerged as a revolutionary transdermal drug delivery system that directly penetrates the stratum corneum to create tiny microporous channels for intradermal drug delivery [15,16]. MNs offer distinct advantages over transdermal patches, enhancing drug delivery efficiency, eliminating the need for extended patch application, and improving patient compliance [17,18]. However, the practical application of MNs faces the challenges of limited bioavailability and low drug loading. In addition, conventional dissolving MNs often fail to provide sustained drug release or prolong the drug's systemic circulation. Given that RVT has a short half-life (approximately 1 h), the loading of free RVT into dissolving MNs may be unable to continuously maintain effective therapeutic plasma concentration; thus, compromising the therapeutic outcomes.

The slow release of drugs from passive MNs usually arises from the gradual hydration of MNs, resulting in a slow rate of drug release, limited penetration depth, and poor bioavailability [19]. Thus, the development of active MNs driven by various tools, such as light, ultrasound, magnetic fields, and gas bubbles, is a promising approach to enhancing drug transdermal permeability and bioavailability. Among these approaches developed for promoting drug permeation into deep skin layers, gas-propelled MNs are more cost-effective and eliminate the need for professional medical or electronic devices, such as lasers or piezoelectric transducers. They load effervescent agents (*e.g.*, K_2CO_3 and citric acid) into the needle tips to generate massive gas bubbles and form a porous structure for accelerating drug release [20–22]. Gas-propelled MNs have demonstrated success in improving the therapeutic efficiency of small molecular therapeutics and biotherapeutics against local skin tumors and systemic illnesses by generating a powerful and autonomous "pumping-like" action [20,23]. However, none of these studies have investigated the effect of introducing effervescent agents into MNs on the pharmacokinetics of the loaded drugs.

Low drug loading is another major obstacle to the practical application of MNs. The tip volume of MNs is typically below 10 μL, making it challenging to load a sufficient drug dose. Moreover, the half-life of RVT is approximately 1 h, indicating that it can be rapidly eliminated *in vivo* and that sustained drug release is preferred for prolonging therapeutic action. Hence, we proposed the loading of highly concentrated drug particles as a drug depot in MNs to simultaneously improve drug loading and achieve sustained drug release. Given that AD is a chronic disease, early intervention is reported to offer potential benefits, such as improving patients' quality of life, extending their lifetime, and reducing overall healthcare costs [24]. However, the currently reported MNs exhibit single drug release behavior, which cannot fulfill the dual functions of early intervention and prolonged treatment through a single administration [25]. Therefore, we proposed the development of bionic gas-propelled MNs as an "all-in-one" strategy to simultaneously address the challenges of low drug loading, poor bioavailability, and unsatisfactory therapeutic outcomes.

Based on the structure of a guava fruit, we co-loaded free RVT and RVT microparticles into dissolving MNs to serve as the valve and chambers of a guava fruit, respectively. Upon insertion into the skin, these MNs absorb water and generate gas bubbles to accelerate the release of free RVT, enabling rapid drug onset and early intervention of AD. As the free RVT is released and the valve collapses, the remaining RVT particles within the MNs create a porous structure that further promotes RVT release by generating capillary force. Thus, we hypothesized that combining effervescent agents and a guava-like structure would yield dual engines of pneumatic and capillary forces to drive the release and permeation of RVT, significantly improving transdermal drug delivery efficiency and bioavailability. Moreover, the RVT particles can sustainably release RVT, enabling prolonged AD treatment, and thus, inhibiting disease progression. Overall, bionic gas-propelled MNs present a promising option for the early intervention and prolonged treatment of AD.

Based on the above knowledge, we aimed to develop bionic MNs driven by the dual engines of pneumatic and capillary forces for early intervention and prolonged treatment of AD (Fig. 1). Specifically, citric acid (CA) and K_2CO_3 were employed as pneumatic initiators to drive the permeation of RVT into deeper skin layers through an acid–base reaction. Free RVT and RVT particles were coloaded into dissolving MNs to construct bionic MNs with a guava-like structure. The bioinspired MN structure was designed to exhibit optimal release behavior, with free RVT enabling rapid drug release for early disease intervention and RVT particles enabling sustained drug release for prolonged treatment. Moreover, formulating RVT into microparticles was expected to address the issue of low drug loading associated with MNs. The gas-propelled MNs, which had high drug loading, were characterized in terms of morphology, drug distribution, dissolvability, release behavior,

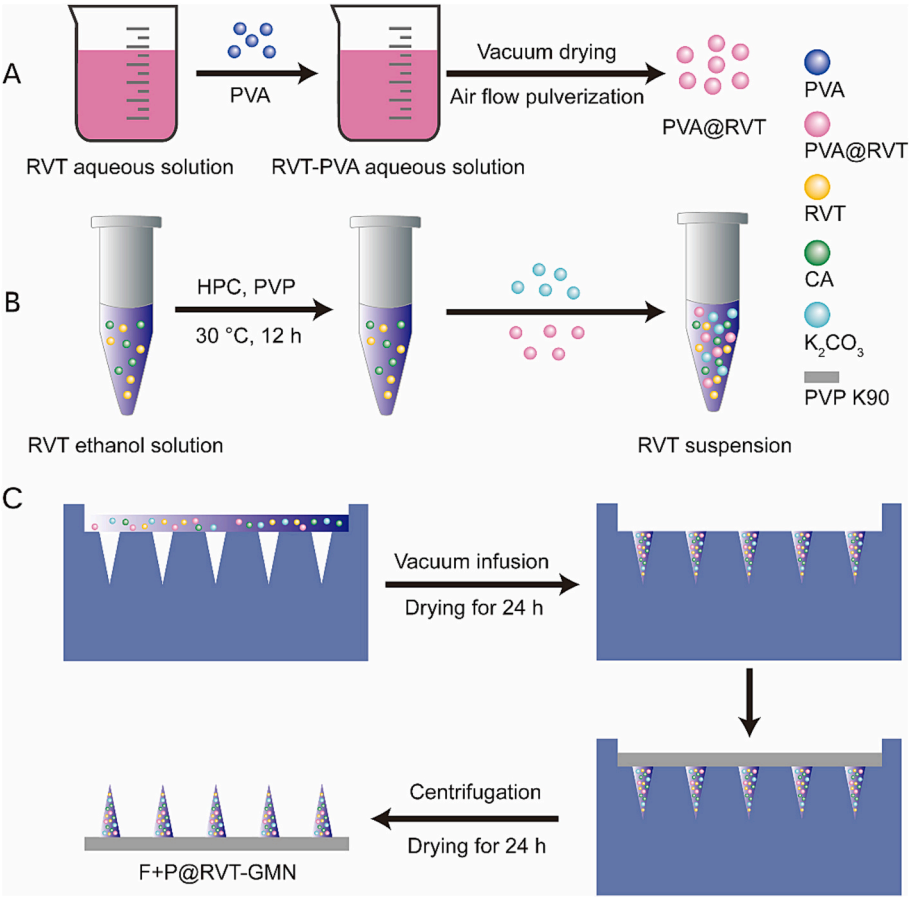

Fig. 2. The schematic illustration of preparing F + P@RVT-GMN.

transdermal permeability, and biodistribution. Finally, pharmacokinetic and pharmacodynamic studies were performed to confirm whether these MNs could enhance the bioavailability of RVT when compared with passive MNs and the commercial product Exelon.

2. Materials and methods

The materials and methods are detailed in the supplementary materials. All the animal experiments conformed to the guidelines approved by the Institutional Animal Care and Use Committee of Sun Yat-sen University (Approval No. SYSU-IACUC-2022-001909).

2.1. Preparation and characterization of MNs

Based on our previous study, a vacuum-based micromolding technology was adopted to prepare RVT-loaded MNs [26]. The preparation process of gas-propelled MNs co-loaded with free RVT and RVT particles (F + P@RVT-GMN) was displayed in Fig. 2, and the detailed formulation compositions of MNs were displayed in Table 1. First, we prepared RVT particles and needle suspension as detailed in the supplementary materials. Then, the needle suspension was filled in the micropores of female mold made from polydimethylsiloxane (PDMS) and degassed under vacuum for 2 min, which were repeated thrice for complete feeding. After the superfluous needle suspension was collected, the female molds were dried at 40 °C for 2 h. Afterwards, PVP K90 ethanol solution (33%, *w*/w) was added into the micropores of the female mold, which was then centrifuged at 4000 rpm and 4 °C for 10 min. Finally, the female mold was dried at 25 °C for 12 h and the F + P@RVT-GMN patches were peeled from the mold for further use. The other three MNs including free RVT-loaded passive MNs (F@RVT-MN), passive MNs co-loaded with free RVT and RVT particles (F + P@RVT-MN), and free RVT-loaded gas-propelled MNs (F@RVT-GMN) were prepared as the same protocol of F + P@RVT-GMN.

Table 1
Formulation compositions of different MNs.

Formulation	Major needle components (g)	CA (g)	K_2CO_3 (g)	PVA@RVT (g)
F@RVT-MN	RVT: Ethanol: HPC: PVP K12: PVP K30: PVP K45 = 0.25:3.0:0.2:0.6:1.2:0.3	/	/	/
F + P@RVT-MN		/	/	0.3
F@RVT-GMN		0.15	0.15	/
F + P@RVT-GMN		0.15	0.15	0.3

2.2. Characterization of MNs

Scanning electron microscope (SEM) (JSM-6330F, JEOL Japan) was used to observe the morphology of MNs and dry film prepared from needle compositions. To prepare fluorescence-labelled MNs, indocyanine green (ICG) and Rhodamine B microparticles (RhB particles) were used to replace free RVT and RVT microparticles, respectively. The correspondent fluorescence-labelled MNs were termed as F@ICG-MN, F@ICG + P@RhB-MN, F@ICG-GMN, and F@ICG + P@RhB-GMN. Confocal laser scanning microscope (CLSM) (Zessi, LSM 710, Jena, Germany) and fluorescence microscope (WIFI1000, Shanghai Renyue Electronic Technology Co., Ltd., Shanghai, China) were further used to visualize the distribution of drug in these MNs. The other physicochemical properties of MNs, including drug loading, mechanical

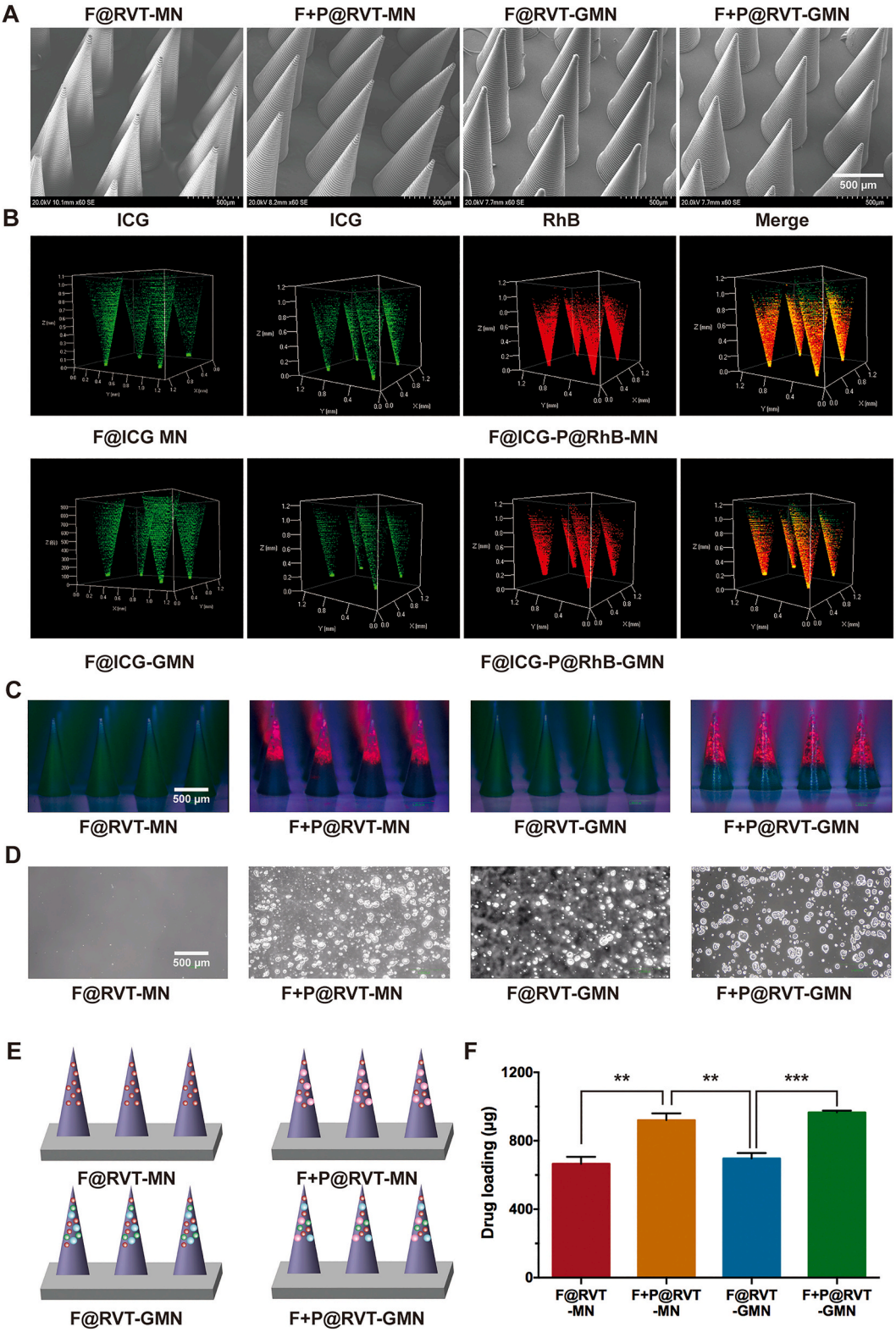

Fig. 3. (A) SEM images of different MNs. (B) CLSM and (C) fluorescence microscope images of different fluorescence-labelled MNs. (D) Optical microscope images of dry film prepared from the needle compositions of MNs. (E) Schematic diagrams and (F) drug loading of different MNs ($n = 3$, $^{**}P<0.01$ and $^{***}P<0.001$).

property, skin penetration ability, gas generation capacity, skin dissolvability, *in vitro* drug release behavior, and *in vitro* transdermal permeability, were characterized according to the methods provided in the supplementary materials.

2.3. *In vitro and in vivo transdermal permeability of MNs*

The fluorescence-labelled MNs, including F@ICG-MN, F@ICG + P@RhB-MN, F@ICG-GMN, and F@ICG + P@RhB-GMN, were inserted into the excised and living rat skin tissues for visualizing the distribution

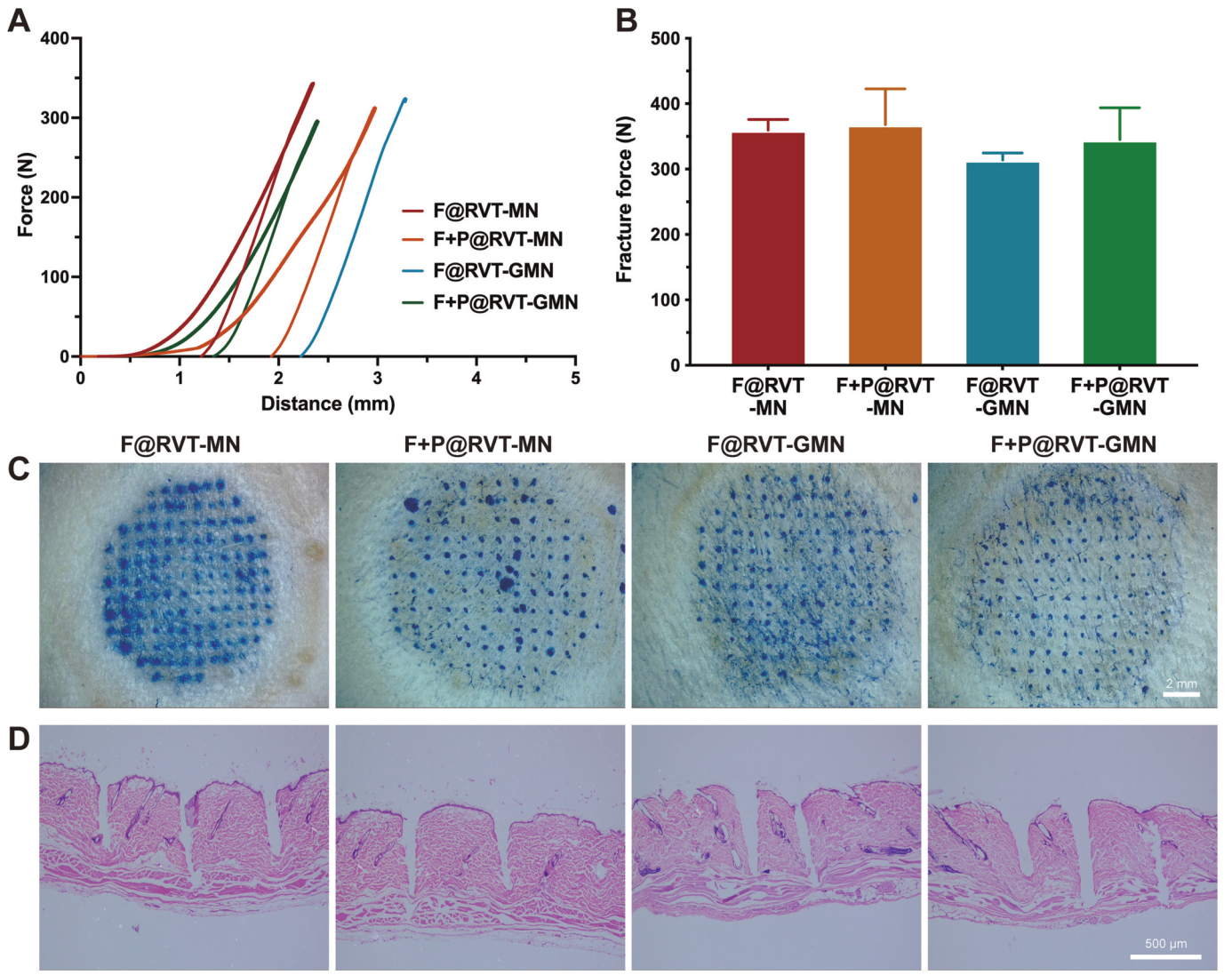

Fig. 4. The mechanical property and skin penetration ability of the MNs. **(A)** Force–displacement curves of MNs applied to the dorsal skin of mice. **(B)** Resultant mechanical strength of different MNs ($n = 3$). **(C)** Trypan blue-stained images and **(D)** H&*E*-stained images of MN-punctured skin tissues. (For interpretation of the references to colour in this figure legend, the reader is referred to the web version of this article.)

of fluorescence agents in the skin layers. The penetration depth and distribution of fluorescence agents at different time points was used as an indicator to evaluate the transdermal permeability of MNs.

2.4. In vivo biodistribution of MNs

To study the biodistribution of drug liberated from different MNs, the F@ICG-MN, F@ICG + P@RhB-MN, F@ICG-GMN, and F@ICG + P@RhB-GMN were applied to the dorsal skin of mice. Then, the living imaging system (IVIS Lumina Series III, Perkinelmer, USA) was used to capture the fluorescent images of mice at predetermined time points. At 8 h post-administration, the mice were sacrificed to collect their major organs for imaging. The resultant fluorescence intensity of dorsal skin or major organs was calculated to evaluate the transdermal delivery efficiency of different MNs.

2.5. Pharmacokinetic study

To conduct the pharmacokinetic study of different preparations, the SD rats were randomly divided into 5 groups (5 mice/group): (1) Exelon patch (650 μg), (2) F@RVT-MN (650 μg), (3) F + P@RVT-MN (900 μg), (4) F@RVT-GMN (650 μg), (5) F + P@RVT-GMN (900 μg). At predetermined time points, the blood samples were taken from the orbital vessels, followed by centrifugation at 5000 rpm for 10 min to collect the plasma. Thereafter, the plasma was extracted using methyl tertiary-butyl ether and 50 ng/mL chlorpheniramine maleate was added to the extracted plasma as an internal standard solution for plasma drug concentration assay by high-performance liquid chromatography–mass spectrometry (HPLC–MS, (Agilent Technologie1100, AB Sciex API 3200).

2.6. Pharmacodynamic evaluation

The Morris water maze test was adopted to study the ability of Exelon or RVT-loaded MNs on restoring the acquisition and memory impairment based on a previous report [25]. The healthy SD rats were randomly divided into 6 groups (6 rats per group): (1) untreated group, (2) Blank MN, (3) Exelon patch (Positive control group), (4) F@RVT-MN, (5) F + P@RVT-MN, and (6) F + P@RVT-GMN. The rats treated with Exelon or MNs were administer once a day for consecutive 12 days. Since the 6th day, the rats were subjected to training at a specific platform for 5 days to familiarize themselves with the pool environment. At day 11, the rats were first administered with different preparations, and then received intraperitoneal injection of scopolamine hydrobromide (1

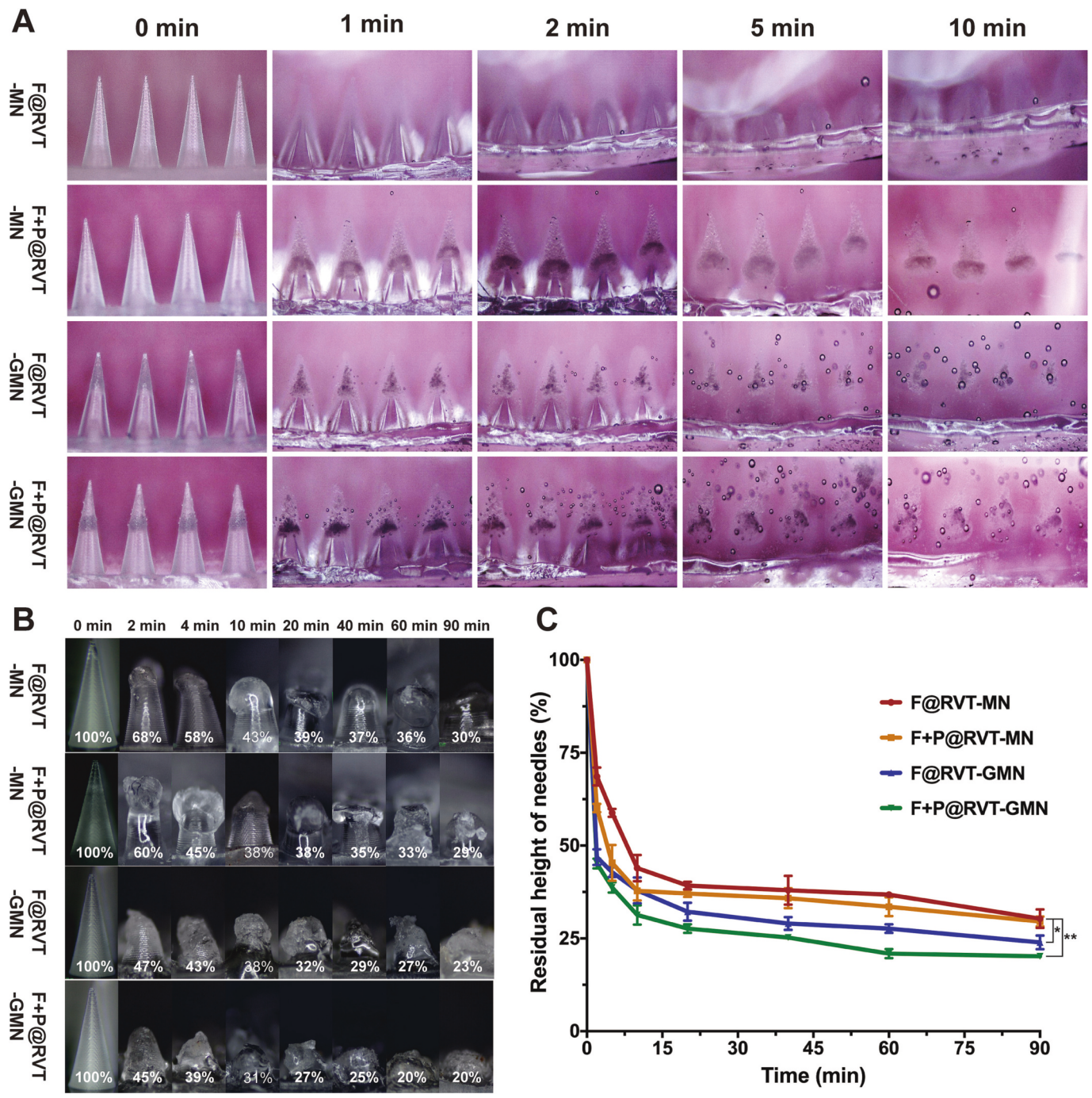

Fig. 5. (A) Optical microscopic images showing the generation of CO_2 bubbles by different MNs. (B) Morphological changes in MNs after insertion into the skin for different time to evaluate their skin dissolvability. (C) The dissolution profiles of different MNs ($n = 3$, $^*P<0.05$ and $^{**}P<0.01$).

mg/kg) at 30 min post-treatment to establish a model of AD with short-term memory deficit. Eighty minutes later, a fixed navigation experiment was performed to record the representative swim paths and escape latency of rats. At day 12, the rats received the same treatments and intraperitoneal injection of scopolamine hydrobromide. Space exploration experiment was then conducted to calculate the frequency of rats crossing the original platform and the retention time of rats in the target quadrant. At the end of experiment, the rats were sacrificed to harvest the cerebral cortex of brain tissues, which was then homogenized and analyzed by rat ELISA kit to determine the level of acetylcholine (ACh), superoxide dismutase (SOD), and malondialdehyde (MDA).

2.7. *In vivo safety study*

The mice receiving MN treatment were sacrificed to harvest the inserted skin tissues at 0, 4, 8, and 24 h post-administration. The skin tissues were sliced and stained with hematoxylin and eosin (H&E) to evaluate whether the MNs caused skin irritation.

3. Results and discussion

3.1. *Preparation and characterization of microneedles*

Based on our previous study, the male mold of MNs was prepared

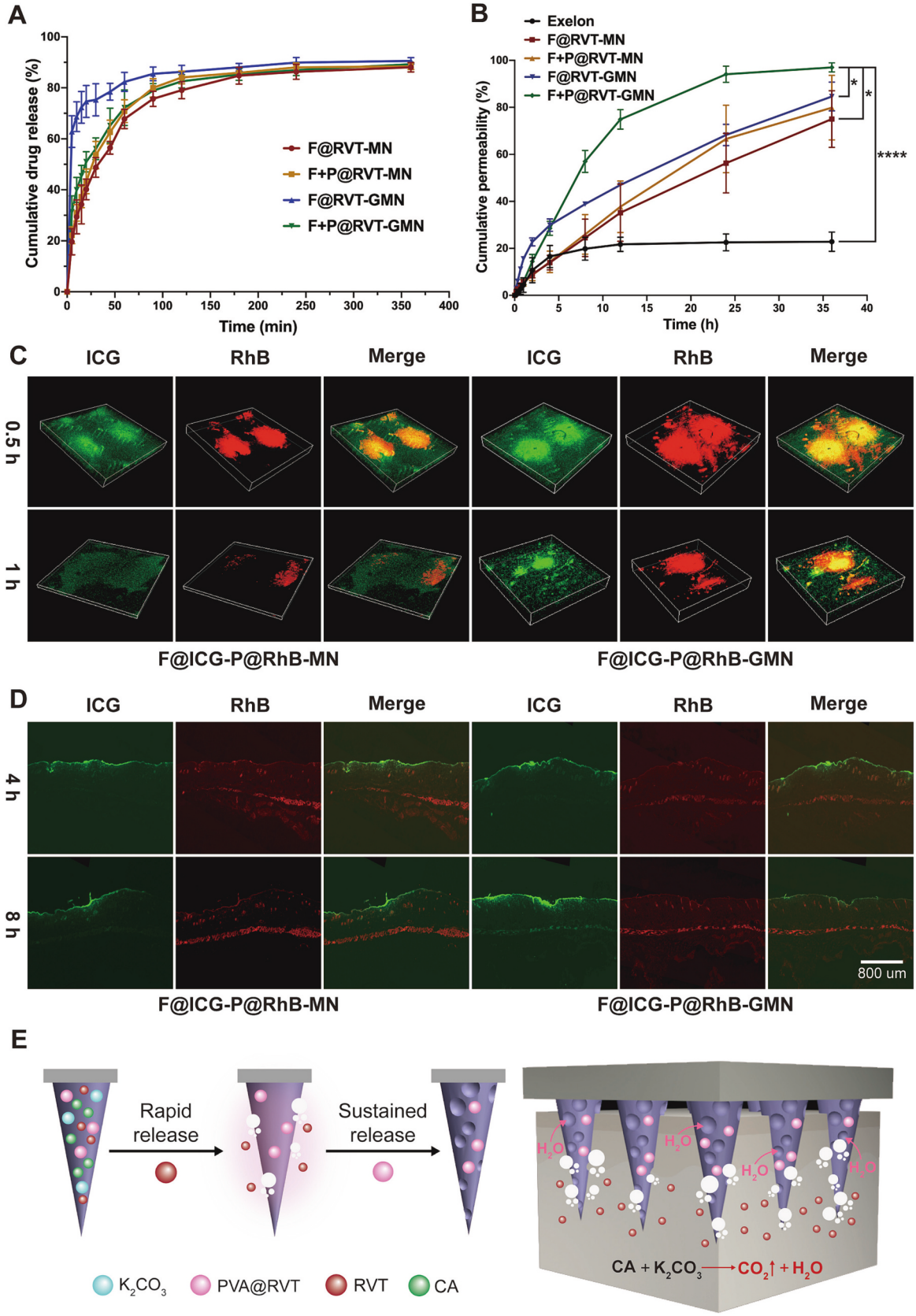

Fig. 6. (A) *In vitro* drug release profiles and (B) Cumulative transdermal permeability curves of different MNs ($n = 3$, $^{*}P<0.05$ and $^{****}P<0.0001$). The permeation of RhB into the (C) excised and (D) living skin tissues to evaluate the transdermal permeability of MNs. (E) Schematic illustrating the integration of effervescent agents and drug particles into MNs to drive the permeation of drug into deep skin layers by generating dual pneumatic and capillary forces.

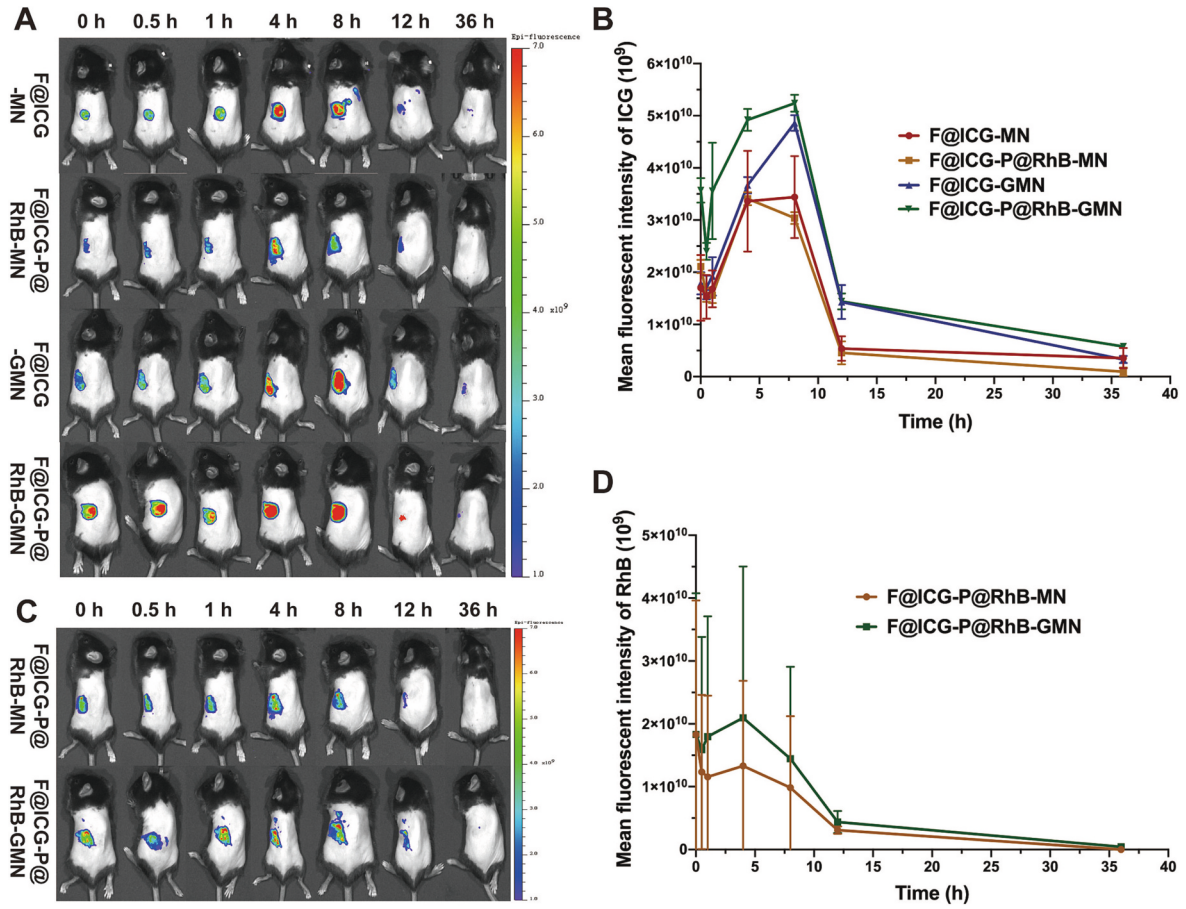

Fig. 7. The fluorescence images and resultant fluorescence intensity of (A–B) ICG and (C—D) RhB accumulated at the dorsal skin of mice treated with different MNs at predetermined time points ($n = 3$).

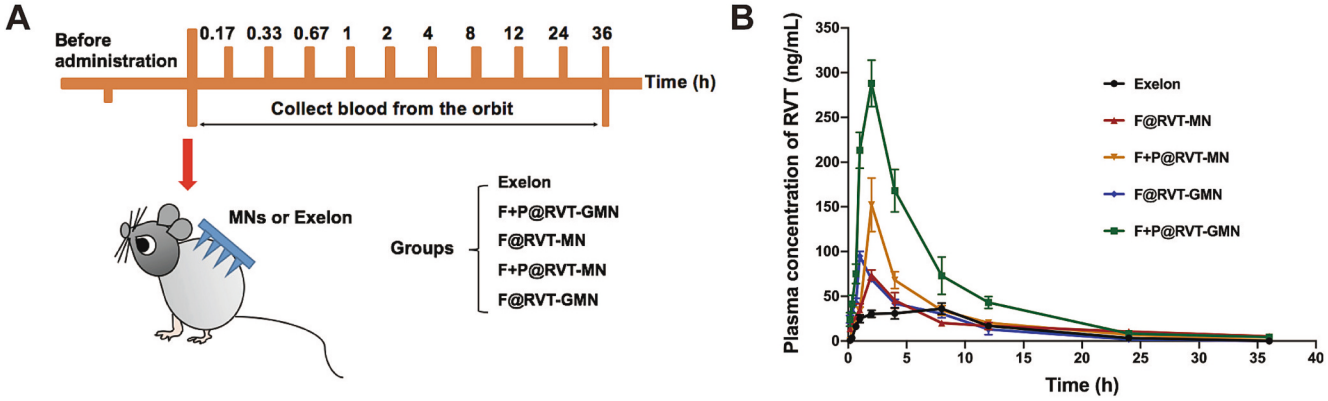

Fig. 8. (A) Experimental design of pharmacokinetic studies, and (B) Pharmacokinetic profiles of Exelon patch and different MNs ($n = 5$).

using projection microstereolithography manufacturing technology, whereas the female mold was prepared by inversely replicating the male mold [26]. Vacuum micromolding technology with optimized pressure was adopted to prepare particle-embedded MNs with superior formability and productivity. Different from centrifugation micromolding technology, this technology can make the needle suspension filled into the micropores of male mold under a pressure gradient, which is mild for the sedimentation of needle suspension and can reduce the separation of particles from polymers caused by gravity [27]. In addition, the matrix materials used to prepare needles were optimized by investigating the effect of PVP K12: PVP K30: PVP K45 at different weight ratios on the productivity of MNs. The needle demolding percentage (DNP) that represents the ratio of the number of intact needles calculated from an optical microscope to that of originally designed needles is used to evaluate the productivity of MNs. The results demonstrated that the MNs prepared from PVP K12, K30, and K45 at the weight ratio of 0.6:1.2:0.3 had intact needle morphology and a highest DNP (Supporting information, Fig. S1). Therefore, we used the optimal formulation compositions to prepare MNs for further study.

The MNs designed in this study were composed of 120 needles and have a tip length of 1200 μm and a tip width of 780 μm. As shown in the SEM images (Fig. 3A), the needles with a conical shape and threaded

Table 2
Pharmacokinetic parameters of Exelon patches and different MNs ($n = 5$).

Parameters	Exelon	F@RVT-MN	F + P@RVT-MN	F@RVT-GMN	F + P@RVT-GMN
Dose(μg)	650	650	900	650	900
T_{max} (h)	8.0	2.0	2.0	1.0	2.0
C_{max} (ng/mL)	36.08 ± 6.30	73.80 ± 5.72	152.20 ± 30.12	94.94 ± 5.25	288.00 ± 26.21
AUC_{0-36} (h·ng/mL)	460.69 ± 61.01	570.33 ± 86.12	830.26 ± 69.94	521.46 ± 55.68	1558.16 ± 214.92
MRT_{0-36} (h)	8.10 ± 0.31	10.93 ± 0.67	7.51 ± 0.74	5.46 ± 1.14	6.81 ± 0.54
$T_{1/2}$ (h)	6.28 ± 1.87	7.64 ± 0.40	6.40 ± 1.09	3.31 ± 1.25	5.24 ± 0.48

texture were regularly arranged on the base. CLSM and fluorescence microscopy were further used to visualize the drug distribution within the MNs and confirm whether the combination of drug particles and free drugs contributed to the formation of guava-like structure. Fig. 3B show that the ICG-derived green fluorescence signal is evenly distributed throughout the needles, whereas the RhB-derived red signal is primarily concentrated on the top of needle tips and partially overlapped with the green fluorescence to form a yellow fluorescence signal. Consistent with the results of CLSM images, the fluorescence microscope images (Fig. 3C) also demonstrate that free drugs are more liable to migrate from the tip to the base than drug particles. In addition, we used the needle compositions of MNs to prepare dry films and observe their morphology by optical microscope. As shown in Fig. 3D, the drug particles are distributed in the dry films as aggregates, which are expected to improve drug loading by impeding drug migration from the needles to the base. Taken together, the distribution of drug particles and free drugs in MNs as a mosaic-like pattern facilitated the construction of MNs with a guava-like structure.

Drug loading is a critical factor that influences the therapeutic efficacy of MNs. To confirm whether the guava-like MNs containing highly drug-concentrated particles could improve drug loading, the drug loading of each MN was determined. Compared with free RVT-loaded MNs (F@RVT-MN and F@RVT-GMN), the drug particle-embedded MNs (F + P@RVT-MN and F + P@RVT-GMN) showed a corresponding increase in drug loading of 30.88% ± 4.61% and 41.18% ± 3.33%, respectively, suggesting that the construction of guava-like MNs effectively improved the drug loading of MNs (Figs. 3E–3F). This result was consistent with previous studies showing that the substitution of free drugs with highly drug-concentrated particles could significantly enhance MN drug loading [28,29]. Another contributing factor to the increased drug loading may be that the drug particles effectively decreased drug migration from the tips to the base of the MNs during drying [30]. No statistically significant difference in drug loading was observed between passive and gas-propelled MNs, implying that adding effervescent agents had no impact on the drug loading of MNs.

3.2. Mechanical strength and skin penetration ability of microneedles

Adequate mechanical strength is the prerequisite for MN-mediated transdermal drug delivery, as it determines whether the MNs can penetrate the skin without breaking [31]. To evaluate the mechanical properties of MNs, we initially used a texture analyzer to record the change of applied force with displacement. During the test, the MNs that were attached to a piece of rat skin were compressed by a pressure probe to record the change of force with descending displacement. The force–displacement curves of MNs (Fig. 4A) show a notable inflection point, indicating where an MN fracture occurred when a certain level of force was applied to them. The resultant fracture forces for F@RVT-MN, F + P@RVT-MN, F@RVT-GMN, and F + P@RVT-GMN were 359.67 ± 16.20 N, 368.01 ± 54.86 N, 313.89 ± 10.59 N, and 345 ± 48.69 N, respectively (Fig. 4B). There is no statistical significance in the mechanical strength of these MNs and all the MNs exhibited a stress level exceeding 0.1 N for each individual needle, which is strong enough to enable the MNs to penetrate the skin [32,33]. Additionally, we used trypan blue staining and H&E staining to evaluate the skin penetration ability of the MNs. Distinct blue spots (Fig. 4C) and clear microholes (Fig. 4D) were observed in all MN-punctured skin tissues. The puncture depth was approximately 450 μm, indicating that the prepared MNs possessed adequate mechanical strength to pierce the skin for intradermal drug delivery.

3.3. Gas generation capacity and skin dissolvability of microneedles

Upon insertion of MNs into the skin, the entry of interstitial fluid into the needle tips triggers a chemical reaction between citric acid and K_2CO_3, producing CO_2 gas bubbles. These bubbles enable the immediate dissolution of the MNs and subsequent drug release [23]. Therefore, we initially evaluated the gas generation capacity of MNs in simulated skin tissue fluid. Compared with the passive MNs, the gas-propelled MNs, such as F@RVT-GMN and F + P@RVT-GMN, produced a substantial amount of CO_2 gas bubbles within 1 min, which increased over time (Fig. 5A). Notably, F + P@RVT-GMN produced larger amounts of gas bubbles than F@RVT-GMN, confirming our hypothesis that combining free RVT and RVT particles to construct bionic MNs with a guava-like structure can increase the water uptake and gas productivity of MNs.

Successful drug release from MNs is critical for the diffusion and permeation of drugs into the dermis, thus enabling systemic drug absorption through dermal capillaries. Hence, the dissolution rate of MNs is a key factor affecting transdermal permeability, pharmacokinetics, and the time needed to reach therapeutic drug levels. The rapid dissolution of MN patches is beneficial for reducing application time and ensuring immediate drug delivery for rapid onset, thereby improving patient compliance. In this study, the skin dissolvability of MNs was monitored by observing the morphological changes of MNs in the excised skin tissues. The remaining height of the MNs was recorded to determine the dissolution rate. The major part of the MNs rapidly dissolved in the skin within 10 min and the remaining portion of the needles slowly dissolved over the next 80 min (Fig. 5B). At 10 min post-administration, the remaining heights of F@RVT-MN, F@RVT-GMN, F + P@RVT-MN, and F + P@RVT-GMN were 43.92% ± 3.54%, 37.80% ± 2.62%, 37.93% ± 3.47%, and 31.33% ± 2.63%, respectively (Fig. 5C). These results indicate that gas-propelled MNs, particularly F + P@RVT-GMN, dissolved more rapidly than passive MNs. Due to the dual engines of gas bubbles and capillary force, F + P@RVT-GMN, with its guava-like structure, demonstrated the most accelerated dissolution. First, F + P@RVT-GMN produced massive gas bubbles, accelerating the disintegration and dissolution of the needles. Second, the guava-like structure of the MNs increased their internal porosity, allowing them to absorb an increased amount of interstitial fluid, which accelerated swelling and dissolution of the polymer matrix *via* capillary force [34]. Despite that the rapid skin dissolvability of gas-propelled MNs can bring potential benefits, the preparation and storage of MNs should be performed under anhydrous conditions to prevent the water uptake of MNs and further chemical reaction between K_2CO_3 and CA [35].

3.4. Drug release behavior and transdermal permeability of microneedles

The *in vitro* drug release profiles of MNs were evaluated using a dialysis method. Within the first 5 min, the cumulative drug release of F@RVT-GMN, F + P@RVT-GMN, F + P@RVT-MN, and F@RVT-MN reached 62.84% ± 6.20%, 31% ± 6.10%, 22% ± 3.31%, and 19% ± 5.12%, respectively (Fig. 6A). Notably, gas-propelled MNs showed a significantly higher drug release rate than passive MNs owing to the propulsion force generated by gas bubbles. The rapid production of massive gas bubbles created an explosive vortex flow acting as an engine that accelerated the disintegration of MNs, enabling rapid drug diffusion into the medium. Compared with free RVT-loaded MNs, integrating RVT

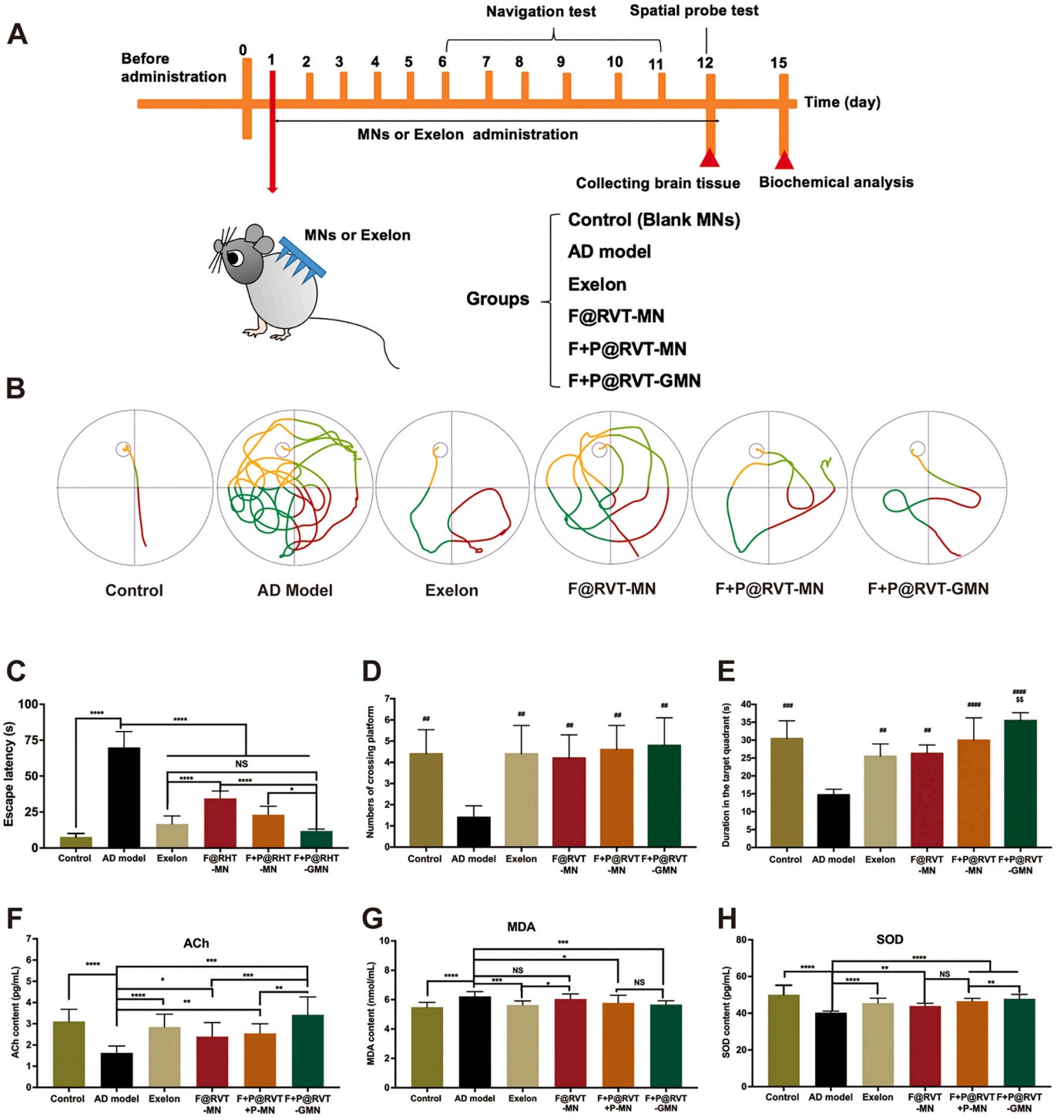

Fig. 9. (A) Schematic illustration of pharmacodynamics studies. Evaluation of different treatments to restore the memory and recognition functions in mice with transient memory deficit ($n = 5$): (B) Representative swim paths, (C) escape latency, (D) numbers of crossing platform, and (E) duration in the target quadrant of rats. Evaluation of different treatments to improve the oxidative stress of AD model mice ($n = 5$): the levels of (F) ACh, (G) MDA, and (H) SOD in the brain tissues of mice. $^{*}P<0.05$, $^{***}P<0.001$, and $^{****}P<0.0001$ *vs* control group; $^{\#\#}P<0.01$ and $^{\#\#\#\#}P<0.0001$ *vs* AD model group; $^{\$\$}P<0.01$ and $^{\$\$\$}P<0.001$vs Exelon group; $^{+}P<0.05$, $^{++}P<0.01$, and $^{+++}P<0.001$ *vs* F@RVT-MN group; $^{\&\&}P<0.01$ *vs* F + P@RVT-MN.

microparticles into MNs efficiently reduced burst release, as the RVT microparticles served as a drug depot to delay drug release by forming a viscous gelling barrier against drug diffusion. F + P@RVT-MN showed a slightly higher drug release rate than F@RVT-MN, suggesting that the guava-like structure of MNs contributed to drug dissolution. An increase in MN porosity has also been reported to facilitate the release of cargo from MNs in previous studies [36,37]. Therefore, we hypothesize that the RVT particles remaining in the MNs form a honeycomb-like porous structure upon the dissolution of free RVT, generating a capillary force that enhances water uptake and accelerates drug release.

A Franz diffusion cell was employed to evaluate the transdermal permeability of Exelon and MNs. RVT gradually released from Exelon and permeated across the skin, reaching a plateau at 12 h. The cumulative transdermal permeability of Exelon was 22.86% ± 4.10%, at 36 h

(Fig. 6B). As compared with Exelon, MNs showed a continuous and significant increase in transdermal permeability, as they can directly penetrate the rigid stratum corneum to create micropores for intradermal drug delivery. In the first 4 h, F@RVT-GMN exhibited the highest cumulative permeability due to its rapid drug release behavior, followed by a decline in drug permeation rate. After 4 h, F + P@RVT-GMN showed significantly higher permeability than F@RVT-GMN at each time point, suggesting that RVT particles could serve as a drug depot to maintain a drug concentration gradient for continuous drug release. Consequently, the final cumulative transdermal permeability of MNs ranked as follows: F + P@RVT-GMN (97.01% ± 1.93%) > F@RVT-GMN (84.64% ± 6.12%) > F + P@RVT-MN (79.88% ± 13.73%) > F@RVT-MN (75.04% ± 12.07%). These results suggested that the combination of effervescent agents and RVT particles to yield dual engines was the most effective in enhancing the drug transdermal permeability of MNs. In addition, the permeability of MNs could be a combined result of drug release behavior and the drug concentration gradient in the local skin tissues.

We further investigated the drug transdermal permeability of MNs in excised and living skin tissues. Compared with passive MNs, gas-propelled MNs promoted a greater amount of drug permeation into deeper skin layers, as evidenced by the stronger fluorescence intensity (Fig. 6C and supporting information, Fig. S2A). The guava-like structure of MNs further increased the drug permeability of F + P@RVT-GMN compared with that of F@RVT-GMN (Fig. 6C). Consistent with the *in vitro* results, the *in vivo* drug permeation study confirmed the combined effect of gas bubbles and the guava-like structure on enhancing the transdermal permeability of MNs (Fig. 6D and supporting information, Fig. S2B).

In conclusion, integrating effervescent agents and drug particles into MNs contributed to higher drug release rates and transdermal permeability of MNs (Fig. 5E). Upon contact with an aqueous medium, effervescent agents undergo an instant chemical reaction to produce massive bubbles that serve as a pneumatic engine to drive the rapid drug release, diffusion, and permeation into the deeper skin layers. After free RVT is released from the MNs, the solid RVT particles embedded in the MNs form a honeycomb-like porous structure, constituting another capillary force-mediated engine that enhances medium infiltration within the MNs for improved drug dissolution. Additionally, RVT particles serve as a drug depot, providing continuous drug release and permeation through the skin, thereby enhancing the transdermal permeability of MNs. Overall, the bionic MNs driven by the dual engines of pneumatic and capillary forces were the most effective in promoting drug transdermal permeability for instant treatment while the drug particles also acted as a depot for continuous treatment.

3.5. Biodistribution of MNs

To further confirm whether the combination of gas-generating ability and guava-like structure of MNs jointly enhanced transdermal delivery efficiency *in vivo*, the IVIS® imaging system was adopted to monitor drug biodistribution in real time. Fluorescence-labelled MNs were prepared to track the dissolution and retention of drugs in the skin, with the fluorescence signals of ICG and RhB representing free RVT and RVT particles, respectively. After administration, strong fluorescence signals were observed on the dorsal skin of mice treated with both passive and gas-propelled MNs (Fig. 7A and C), showing successful delivery of ICG and RhB to the skin. The fluorescence intensity of ICG accumulated at the dorsal skin rapidly increased with administration time, reaching a peak at 4 and 8 h for the passive MNs and gas-propelled MNs, respectively (Figs. 7A–7B). Subsequently, the fluorescence intensity of all the mice gradually decreased over time, with the F + P@RVT-GMN group retaining the highest fluorescence radiant efficiency (approximately 11.73% ± 3.75%) at 36 h. The changes in RhB fluorescence intensity (Figs. 7C–7D) over time followed a similar trend to that of ICG, and a larger amount of RhB accumulated in the major organs was obtained in the gas-propelled MNs (Supporting information, Fig. S3). Generally, gas-propelled MNs showed significantly higher fluorescence intensity than passive MNs at each time point, indicating that the gas propellant could generate a distinct vortex flow to enhance drug permeation into deeper skin layers [20,22,23]. Moreover, these results demonstrated that the release of free RVT increased as the MNs dissolved, whereas the RVT particles served as a drug reservoir to provide continuous drug release, thereby enhancing systemic drug absorption and bioavailability [38]. Therefore, the F + P@RVT-GMN patches offer a promising alternative to commercial Exelon patches, reducing patching time and increasing patient compliance.

3.6. Pharmacokinetic studies

The plasma concentration of RVT was determined usingHPLC–MS to obtain the pharmacokinetic profiles for the Exelon patch and various MNs (Fig. 8A–B). All the MNs showed an increase in plasma drug concentration, reaching a peak within the first 1–2 h due to rapid drug absorption into the bloodstream, followed by a decline due to drug elimination from the body. In contrast, Exelon required 8 h to reach its peak concentration, as the transdermal patch struggled to overcome the stratum corneum barrier, resulting in slower drug transdermal permeation and systemic absorption. F@RVT-MN have a maximum peak concentration of 73.8 ng/mL, which is 2-fold of the Exelon patch (36.08 ng/mL). This result demonstrated that MNs, at an equivalent dose to the Exelon patch, enable faster transdermal drug absorption, allowing the drug to rapidly reach its therapeutic concentration window. In addition, F + P@RVT-GMN and F + P@RVT-MN showed continuous, systematic drug absorption, maintaining plasma concentrations above 40 and 20 ng/mL for over 12 h, respectively, suggesting that the drug particles served as a microreservoir to prolong drug circulation for prolonged treatment. Compared with passive MNs, gas-propelled MNs produced higher plasma concentrations, confirming the ability of pneumatic engines to enhance drug bioavailability. In particular, F + P@RVT-GMN showed significantly higher plasma drug concentrations than F@RVT-MN, particularly in the first 5 h, which allows for early intervention in AD. Moreover, the normalized peak plasma concentration of F + P@RVT-GMN was 1.38-fold of F@RVT-GMN, confirming the role of capillary force in enhancing the transdermal drug delivery efficiency. These results substantially demonstrated the immense potential of F + P@RVT-GMN for highly efficient AD treatment, as it not only provided higher bioavailability but also ensured continuous systemic drug absorption within 24 h. The MNs also overcome the common shortcomings of traditional transdermal patches, such as low bioavailability, high drug dosage, and the need for long patching times (24 h) to achieve certain therapeutic outcomes [39].

The primary pharmacokinetic parameters of Exelon and the MNs are shown in Table 2. C_{max} represents the maximum drug concentration achieved in a specified compartment [21]. Compared with Exelon, the C_{max} values of all MN groups were significantly increased and ranked as follows: F + P@RVT-GMN (288.00 ± 26.21 ng/mL) > F + P@RVT-MN (152.20 ± 30.12 ng/mL) > F@RVT-GMN (94.94 ± 5.25 ng/mL) > F@RVT-MN (73.80 ± 5.72 ng/mL). The area under the plasma drug concentration *versus* time curve (AUC) reflects the overall exposure to a drug in the systemic circulation over time [40]. A higher AUC typically results from higher transdermal delivery efficiency of the preparations, leading to superior therapeutic outcomes. No statistically significant difference was observed in the AUC of Exelon (460.69 ± 61.01 ng·h/mL) and F@RVT-MN (570.33 ± 86.12 ng·h/mL). However, normalized AUC values significantly increased in both gas-propelled and drug particle-embedded MNs. Particularly, the normalized AUC value of F + P@RVT-GMN showed a 2.44-fold increase compared with that of Exelon patches. The mean residence time (MRT) of drugs in the body the time required to eliminate half of the administered drug dosage ($T_{1/2}$) from the body followed the same order: F@RVT-MN > Exelon > F + P@RVT-MN > F + P@RVT-GMN > F@RVT-GMN. These results suggest that (1)

slower drug permeation across the skin led to longer MRT and $T_{1/2}$; (2) engines derived from gas bubbles and capillary force facilitated drug permeation for more rapid systemic absorption, thereby resulting in shorter MRT and $T_{1/2}$; and (3) formulation of drug into particles effectively prolonged drug circulation to provide prolonged treatment. In summary, gas-propelled MNs with a guava-like structure can leverage the dual engines of pneumatic and capillary forces to substantially increase the transdermal permeability and bioavailability of RVT. Consequently, F@RVT-GMN emerges as a superior option to Exelon patches for the continuous treatment of AD.

3.7. Pharmacodynamic evaluation

AD is a common neurodegenerative disorder that primarily affects the elderly and typically causes learning and memory dysfunction [25]. Decreased ACh content in brain neurons is a pathological hallmark of AD, severely impairing information transmission-processing and memory functions in patients [41]. The imbalance between oxidative and antioxidant systems is another major feature of AD, resulting in decreased levels of SOD and increased accumulation of MDA. SOD is a critical antioxidant enzyme that helps eliminate excessive oxygen free radicals in the brain to protect neurons from oxidative damage [42]. Conversely, MDA is a specific degradation product of lipid peroxidation that correlates positively with the degree of cell damage [43]. Therefore, the learning acquisition and memory function in model rats, as well as the levels of ACh, SOD, and MDA in the brain tissues, were determined to evaluate the therapeutic efficacy of different treatments (Fig. 9A).

After 5 days of consecutive treatments, the rats were trained to locate the target quadrant of a pool through a positioning navigation test. As the training sessions progressed from days 6–10, all groups showed a gradual decline in escape latency, with no statistically significant differences observed at the endpoint (Supporting information, Fig. S4). This finding suggested that all the rats learned to find a specific platform and exhibited similar learning and memory abilities after 5 days of training. At day 11, the mice were intraperitoneally injected with scopolamine to establish a transient memory deficit model that mimics the progression of AD [25]. Forty minutes later, a Morris water maze test was conducted to record the swim paths and escape latency of model rats as indicators of memory function. The typical swim paths of each group demonstrated that the mice injected with scopolamine developed short-term memory deficits, resulting in random and chaotic swimming trails (Fig. 9B). Inspiringly, F + P@RVT-GMN was most effective in improving the memory function of model mice as evidenced by the shortest swimming distance and fastest swimming velocity (Fig. 9B). In addition, the escape latency of scopolamine-induced rats was significantly increased and then reduced to varying degrees after receiving Exelon or MN treatments (Fig. 9C). Particularly, the escape latency of F + P@RVT-GMN-treated rats approached normal levels, indicating superior memory repair compared with the Exelon and F@RVT-MN groups.

At day 12, a probe trial was performed to detect the spatial learning and memory abilities of the mice. After consecutive treatments with MNs or Exelon, the number of mice crossing the original platform (Fig. 9D) and the time spent in the target quadrant (Fig. 9E) increased significantly compared with those of the model group. The retention time of rats in the target quadrant followed the order of F + P@RVT-GMN (35.46 ± 2.20 s) > Control (30.42 ± 4.98 s) ≈ F + P@RVT-MN (29.98 ± 6.25 s) > F + P@RVT (26.28 ± 2.40 s) ≈ Exelon (25.50 ± 3.44 s) > AD model (14.68 ± 1.58 s), indicating that F + P@RVT-GMN was the most effective treatment in improving the spatial learning and memory abilities of AD mice. After the experiment, the brain tissues of mice were harvested to determine ACh content and oxidative stress levels. Compared with the model mice, the treated mice showed a significant increase in ACh (Fig. 9F) and SOD (Fig. 9G) levels, with the ranking as follows: F + P@RVT-GMN > Exelon ≥ F + P@RVT-MN ≥ F@RVT-MN. Conversely, MDA levels (Fig. 9H) dramatically decreased in the treatment groups. These results collectively demonstrated that F + P@RVT-GMN was the most effective therapeutic regimen for alleviating AD symptoms by improving cognitive and memory functions and decreasing oxidative stress levels. If the MNs are endowed with long-acting drug release behavior, they will provide long-term therapy for the patients with neurodegenerative diseases, thus reducing dose frequency and improving patient compliance.

3.8. Skin irritation

A satisfactory MN product should exert no or negligible irritation on the skin. Therefore, we performed visual inspection and histopathological analysis to evaluate whether MNs caused skin irritation. During administration, slight skin erythema was observed due to the puncture force of the MNs, but it gradually disappeared over time. Additionally, no notable signs of cortical edema or inflammatory cell infiltration were observed in any of the MN treatment groups (Supporting information, Fig. S5). These results indicate that the developed MNs exhibited good biocompatibility and caused no skin irritation.

4. Conclusion

In summary, this study presented the development of dual engine-driven bionic MNs to effectively address common challenges associated with conventional MNs, including low drug loading, intermittent drug release, and limited delivery efficiency. Inspired by the structure of guava, the co-loading of free RVT and RVT particles in MNs significantly improved drug loading, which was increased by about 40% as compared to that of free RVT-loaded MNs. In contrast with Exelon, these MNs also provided continuous drug release and systemic absorption for the prolonged treatment of AD, as the time for *in vitro* transdermal drug permeation was extended from 12 h to 36 h. Furthermore, the biomimetic structure of MNs synergized with gas bubbles to promote drug release and permeation into deeper skin layers through dual capillary and pneumatic driving forces. Compared with F@RVT-MNs, the biomimetic gas-propelled MNs (F + P@RVT-GMNs) significantly enhanced transdermal permeability and bioavailability, which show an increase approaching to 22% and 49%, respectively. The pharmacodynamic study demonstrated that the biomimetic gas-propelled MNs offered superior therapeutic efficiency to conventional MNs and Exelon, highlighting the potential benefits of the biomimetic structure and gas bubbles in improving drug release kinetics and drug delivery efficiency. These results collectively demonstrate the great potential of guava-inspired and gas-propelled MNs for treating neurodegenerative diseases.

CRediT authorship contribution statement

Minmin Zhang: Writing – original draft, Project administration, Data curation, Conceptualization. **Beibei Yang:** Writing – original draft, Software, Data curation. **Tao Ren:** Software, Project administration. **Xuewen Wang:** Software, Project administration. **Hangping Chen:** Visualization, Software. **Chao Lu:** Visualization, Software. **Chuanbin Wu:** Writing – review & editing, Supervision, Funding acquisition. **Xin Pan:** Writing – review & editing, Supervision, Funding acquisition. **Tingting Peng:** Writing – review & editing, Supervision, Funding acquisition, Conceptualization.

Declaration of competing interest

The authors have no conflicts of interest to declare.

Data availability

Data will be made available on request.

Acknowledgements

This work was supported by National Natural Science Foundation of China (82104071, 82330112), Natural Science Foundation of Guangdong Province (2022B1515020085), Research Project of Guangdong Provincial Bureau of Traditional Chinese Medicine (20231084), and Leading Entrepreneurship Team Project of Zengcheng District (202001004).

Appendix A. Supplementary data

Materials and methods adopted to prepare and characterize MNs; The characterization of MNs includes drug loading, gas generation capacity, skin dissolvability, *in vitro* drug release behavior, and *in vitro* transdermal permeability of MNs; The ability of dual engine-driven bionic MNs to enhance transdermal permeability was evaluated in terms of biodistribution, pharmacokinetics, and pharmacodynamics; Statistical analysis; Figures showing the influence of needle compositions on the productivity of MNs, the distribution of RhB in the major organs and resultant fluorescent intensity, escape latency of mice after training in the Morris water maze test for different time, and the H&E staining of MN-treated skin to demonstrate the skin irritation of MNs; Table displaying the formulation compositions of different MNs.

References

[1] J. Graff-Radford, K.X.X. Yong, L.G. Apostolova, F.H. Bouwman, M. Carrillo, B. C. Dickerson, G.D. Rabinovici, J.M. Schott, D.T. Jones, M.E. Murray, New insights into atypical Alzheimer's disease in the era of biomarkers, Lancet Neurol. 20 (2021) 222–234.
[2] H. Inuzuka, J. Liu, W. Wei, A.H. Rezaeian, PROTACs technology for treatment of Alzheimer's disease: advances and perspectives, Acta Mater. Med. 1 (2022) 24–41.
[3] C. Tudose, S. Paveliu, P4-362: health resources usage and cost of Alzheimer's disease in a cohort of ambulatory patients registred at Bucharest memory center, Alzheimers Dement. 8 (2012).
[4] C.A. Lane, J. Hardy, J.M. Schott, Alzheimer's disease, Eur. J. Neurol. 25 (2018) 59–70.
[5] D.F. Zhang, M. Xu, R. Bi, Y.G. Yao, Genetic analyses of Alzheimer's disease in China: achievements and perspectives, ACS Chem. Neurosci. 10 (2019) 890–901.
[6] A.K. Sahoo, J. Dandapat, U.C. Dash, S. Kanhar, Features and outcomes of drugs for combination therapy as multi-targets strategy to combat Alzheimer's disease, J. Ethnopharmacol. 215 (2018) 42–73.
[7] R. Cacabelos, Pharmacogenetic considerations when prescribing cholinesterase inhibitors for the treatment of Alzheimer's disease, Expert Opin. Drug Metab. Toxicol. 16 (2020) 673–701.
[8] C.C. Zhu, S.Y. Fu, Y.X. Chen, L. Li, R.L. Mao, J.Z. Wang, R. Liu, Y. Liu, X.C. Wang, Advances in drug therapy for Alzheimer's disease, Curr. Med. Sci. 40 (2020) 999–1008.
[9] N. Cortes, K. Sierra, F. Alzate, E.H. Osorio, E. Osorio, Alkaloids of Amaryllidaceae as inhibitors of cholinesterases (AChEs and BChEs): an integrated bioguided study, Phytochem. Anal. 29 (2018) 217–227.
[10] R. Ren, J. Qi, S. Lin, X. Liu, P. Yin, Z. Wang, R. Tang, J. Wang, Q. Huang, J. Li, X. Xie, Y. Hu, S. Cui, Y. Zhu, X. Yu, P. Wang, Y. Zhu, Y. Wang, Y. Huang, Y. Hu, Y. Wang, C. Li, M. Zhou, G. Wang, The China Alzheimer report 2022, Gen. Psychiat. 35 (2022) e100751.
[11] A. Simon, M.I. Amaro, L.M. Cabral, A.M. Healy, V.P. de Sousa, Development of a novel dry powder inhalation formulation for the delivery of rivastigmine hydrogen tartrate, Int. J. Pharm. 501 (2016) 124–138.
[12] Y. Cai, Q. Tian, C. Liu, L. Fang, Development of long-acting rivastigmine drug-in-adhesive patch utilizing ion-pair strategy and characterization of controlled release mechanism, Eur. J. Pharm. Sci. 161 (2021) 105774.
[13] T. Osada, N. Watanabe, N. Asano, Y. Adachi, K. Yamamura, Adverse drug events affecting medication persistence with rivastigmine patch application, Patient Prefer. Adherence 12 (2018) 1247–1252.
[14] G. Alva, J.L. Cummings, J.E. Galvin, X. Meng, D.M. Velting, Skin reactions at the application site of rivastigmine patch (4.6 mg/24 h, 9.5 mg/24 h or 13.3 mg/24 h): a qualitative analysis of clinical studies in patients with Alzheimer's disease, Int. J. Clin. Pract. 69 (2015) 518–530.
[15] Y. Gu, Q. Bian, Y. Zhou, Q. Huang, J. Gao, Hair follicle-targeting drug delivery strategies for the management of hair follicle-associated disorders, Asian, J. Pharm. Sci. 17 (2022) 333–352.
[16] Y. Zhang, Y. Xu, H. Kong, J. Zhang, H.F. Chan, J. Wang, D. Shao, Y. Tao, M. Li, Microneedle system for tissue engineering and regenerative medicine, Exploration 3 (2023) 20210170.
[17] I.K. Ramoller, I.A. Tekko, H.O. McCarthy, R.F. Donnelly, Rapidly dissolving bilayer microneedle arrays - a minimally invasive transdermal drug delivery system for vitamin B12, Int. J. Pharm. 566 (2019) 299–306.
[18] M. Wu, T. Xia, Y. Li, T. Wang, S. Yang, J. Yu, Q. Liang, T. Shen, M. Yu, B. Zhao, Design and fabrication of r-hirudin loaded dissolving microneedle patch for minimally invasive and long-term treatment of thromboembolic disease, Asian, J. Pharm. Sci. 17 (2022) 284–297.
[19] J. You, C. Yang, J. Han, H. Wang, W. Zhang, Y. Zhang, Z. Lu, S. Wang, R. Cai, H. Li, J. Yu, J. Gao, Y. Zhang, Z. Gu, Ultrarapid-acting microneedles for immediate delivery of biotherapeutics, Adv. Mater. 35 (2023) e2304582.
[20] P. Liu, Y. Fu, F. Wei, T. Ma, J. Ren, Z. Xie, S. Wang, J. Zhu, L. Zhang, J. Tao, J. Zhu, Microneedle patches with O_2 propellant for deeply and fast delivering photosensitizers: towards improved photodynamic therapy, Adv. Sci. 9 (2022) e2202591.
[21] F. Volpe-Zanutto, L.K. Vora, I.A. Tekko, P.E. McKenna, A.D. Permana, A.H. Sabri, Q.K. Anjani, H.O. McCarthy, A.J. Paredes, R.F. Donnelly, Hydrogel-forming microarray patches with cyclodextrin drug reservoirs for long-acting delivery of poorly soluble cabotegravir sodium for HIV pre-exposure prophylaxis, J. Control. Release 348 (2022) 771–785.
[22] M.A. Lopez-Ramirez, F. Soto, C. Wang, R. Rueda, S. Shukla, C. Silva-Lopez, D. Kupor, D.A. McBride, J.K. Pokorski, A. Nourhani, N.F. Steinmetz, N.J. Shah, J. Wang, Built-in active microneedle patch with enhanced autonomous drug delivery, Adv. Mater. 32 (2020) e1905740.
[23] X. Ning, S. Chen, Y. Yang, J. Hwang, C. Wiraja, C. Zhang, W. Liu, L. Liu, C. Xu, Photodynamic bubble-generating microneedles for enhanced transdermal cancer therapy, ACS Appl. Polym. Mater. 3 (2021) 6502–6512.
[24] J.H. Barnett, L. Lewis, A.D. Blackwell, M. Taylor, Early intervention in Alzheimer's disease: a health economic study of the effects of diagnostic timing, BMC Neurol. 14 (2014) 101.
[25] Q. Yan, W. Wang, J. Weng, Z. Zhang, L. Yin, Q. Yang, F. Guo, X. Wang, F. Chen, G. Yang, Dissolving microneedles for transdermal delivery of huperzine a for the treatment of Alzheimer's disease, Drug Deliv. 27 (2020) 1147–1155.
[26] M. Zhang, B. Yang, X. Luan, L. Jiang, C. Lu, C. Wu, X. Pan, T. Peng, State of the art in constructing gas-propelled dissolving microneedles for significantly enhanced drug loading and delivery efficiency, Pharmaceutics 15 (2023) 1059.
[27] H. Chen, B. Wu, M. Zhang, P. Yang, B. Yang, W. Qin, Q. Wang, X. Wen, M. Chen, G. Quan, X. Pan, C. Wu, A novel scalable fabrication process for the production of dissolving microneedle arrays, Drug Deliv. Transl. Res. 9 (2019) 240–248.
[28] M. Jang, B.M. Kang, H. Yang, J. Ohn, O. Kwon, H. Jung, High-dose steroid dissolving microneedle for relieving atopic dermatitis, Adv. Healthc. Mater. 10 (2021) e2001691.
[29] I.A. Tekko, A.D. Permana, L. Vora, T. Hatahet, H.O. McCarthy, R.F. Donnelly, Localised and sustained intradermal delivery of methotrexate using nanocrystal-loaded microneedle arrays: potential for enhanced treatment of psoriasis, Eur. J. Pharm. Sci. 152 (2020) 105469.
[30] Q. Wang, G. Yao, P. Dong, Z. Gong, G. Li, K. Zhang, C. Wu, Investigation on fabrication process of dissolving microneedle arrays to improve effective needle drug distribution, Eur. J. Pharm. Sci. 66 (2015) 148–156.
[31] W. Hu, T. Peng, Y. Huang, T. Ren, H. Chen, Y. Chen, D. Feng, C. Wu, X. Pan, Hyaluronidase-powered microneedles for significantly enhanced transdermal delivery efficiency, J. Control. Release 353 (2023) 380–390.
[32] S.P. Davis, B.J. Landis, Z.H. Adams, M.G. Allen, M.R. Prausnitz, Insertion of microneedles into skin: measurement and prediction of insertion force and needle fracture force, J. Biomech. 37 (2004) 1155–1163.
[33] D.D. Zhu, B.Z. Chen, M.C. He, X.D. Guo, Structural optimization of rapidly separating microneedles for efficient drug delivery, J. Ind. Eng. Chem. 51 (2017) 178–184.
[34] M.H. Ya Gao, Ruihao Yang, Lei Zhang, Xu Zhigang, Yuejun Kang, A.P. Xue, Highly porous silk fibroin scaffold packed in PEGDA/sucrose microneedles for controllable transdermal drug delivery, Biomacromolecules 20 (2019) 1334–1345.
[35] W. Li, J. Tang, R.N. Terry, S. Li, A. Brunie, R.L. Callahan, R.K. Noel, C. A. Rodriguez, S.P. Schwendeman, M.R. Prausnitz, Long-acting reversible contraception by effervescent microneedle patch, Sci. Adv. 5 (2019) eaaw8145.
[36] P.J. Vos, N. Kuijt, M. Kaya, S. Rol, K. van der Maaden, Nanoporous microneedle arrays seamlessly connected to a drug reservoir for tunable transdermal delivery of memantine, Eur. J. Pharm. Sci. 150 (2020) 105331.
[37] A. Fang, Y. Wang, N. Guan, Y. Zuo, L. Lin, B. Guo, A. Mo, Y. Wu, X. Lin, W. Cai, X. Chen, J. Ye, Z. Abdelrahman, X. Li, H. Zheng, Z. Wu, S. Jin, K. Xu, Y. Huang, X. Gu, B. Yu, X. Wang, Porous microneedle patch with sustained delivery of extracellular vesicles mitigates severe spinal cord injury, Nat. Commun. 14 (2023) 4011.
[38] Z. Men, T. Su, Z. Tang, J. Liang, T. Shen, Tacrolimus nanocrystals microneedle patch for plaque psoriasis, Int. J. Pharm. 627 (2022) 122207.
[39] J.W. So, H.H. Park, S.S. Lee, D.C. Kim, S.C. Shin, C.W. Cho, Effect of microneedle on the pharmacokinetics of ketoprofen from its transdermal formulations, Drug Deliv. 16 (2009) 52–56.
[40] Y.A. Naser, I.A. Tekko, L.K. Vora, K. Peng, Q.K. Anjani, B. Greer, C. Elliott, H. O. McCarthy, R.F. Donnelly, Hydrogel-forming microarray patches with solid dispersion reservoirs for transdermal long-acting microdepot delivery of a hydrophobic drug, J. Control. Release 356 (2023) 416–433.
[41] T.H. Ferreira-Vieira, I.M. Guimaraes, F.R. Silva, F.M. Ribeiro, Alzheimer's disease: targeting the cholinergic system, Curr. Neuropharmacol. 14 (2016) 101–115.
[42] M. Naziroglu, S. Muhamad, L. Pecze, Nanoparticles as potential clinical therapeutic agents in Alzheimer's disease: focus on selenium nanoparticles, Expert. Rev. Clin. Pharmacol. 10 (2017) 773–782.
[43] M.W. Park, H.W. Cha, J. Kim, J.H. Kim, H. Yang, S. Yoon, N. Boonpraman, S.S. Yi, I.D. Yoo, J.S. Moon, NOX4 promotes ferroptosis of astrocytes by oxidative stress-induced lipid peroxidation via the impairment of mitochondrial metabolism in Alzheimer's diseases, Redox Biol. 41 (2021) 101947.